

# Simulation Studies on Hydrogen Sorption and Its Thermodynamics in Covalently Linked Carbon Nanotube Scaffold

Mousumi Mani Biswas and Tahir Cagin\*

Artie McFerrin Department of Chemical Engineering, and Department of Materials Science & Engineering, Texas A&M University, College Station, Texas 77845-3122 United States

Received: March 28, 2010; Revised Manuscript Received: July 30, 2010

Carbon nanotubes are potential hydrogen storage materials because of their large surface area and high sorbate–surface interaction energy due to the curvature effect. However, single walled carbon nanotubes bundle up tightly, so most of their surface areas become inaccessible for adsorption. As a solution, spacer molecules can be used to hold the tubes at a distance from each other in a scaffolded structure. Here, using grand canonical Monte Carlo simulation, we show that scaffolds can achieve high sorption capacity. We analyze the sorption capacity of (6, 6), (9, 9), (12, 12), (15, 15), (18, 18), and (21, 0) tube scaffolds with linker distances along the *c*-axis ranging from 8.14 to 24.4 Å, as a function of tube diameter and spacer density, for various temperatures and pressures. In order to explore additional avenues to further improve the sorption capacity, we studied surface functionalized and Li<sup>+</sup> ion decorated nanotube scaffolds. We also report the thermodynamics of sorption based on isosteric heat.

## 1. Introduction

Hydrogen has three times higher energy content (142 MJ/kg) compared to liquid hydrocarbons (47 MJ/kg). It can be generated from various renewable resources and has no adverse effect on the environment when used as a fuel. Therefore, hydrogen has the potential to replace rapidly depleting hydrocarbons as an energy source.<sup>1,2</sup> However, hydrogen has four times lower volumetric energy density (8 MJ/L) compared to liquid hydrocarbons (32 MJ/L) at normal temperature and pressure.<sup>3</sup> So the main challenge is how to store a large amount of hydrogen within a limited space to achieve similar energy density as the hydrocarbon fuels. This will enable use of hydrogen as an alternative fuel, especially in the transport sector.

To address this storage problem, traditionally, hydrogen fuel is liquefied and compressed to obtain practical volumetric energy densities. However, such liquefaction and compression is energy intensive (up to 30% of the stored energy in the hydrogen is lost).<sup>3</sup> Therefore, the researchers in this field are striving to develop alternative, energy inexpensive, adsorption based storage strategies. Various high adsorption capacity materials, like metal hydrides, metal organic frameworks (MOFs), and various carbon nanostructures are being actively investigated.

Carbon nanostructures such as single walled and multiwalled carbon nanotubes (SWNTs, MWNTs), fullerene, graphene, etc., have gained considerable interest<sup>4–11</sup> after Dillon et al.<sup>4</sup> demonstrated some promising results regarding hydrogen storage potential of SWNTs. Carbon nanotubes (CNTs) are particularly attractive because, in addition to the porosity and large surface area, curved surface and capillary effect may further increase the H<sub>2</sub> storage capacity.<sup>12</sup> However, the adsorption on “plain” carbon nanotubes does not reach the necessary storage capacity as targeted by the U.S. DOE (6 wt % gravimetric capacity at a temperature range of –30 to 50 °C).<sup>3</sup> Fortunately, there are several avenues which may be investigated to improve the adsorption capacity of CNT structures.

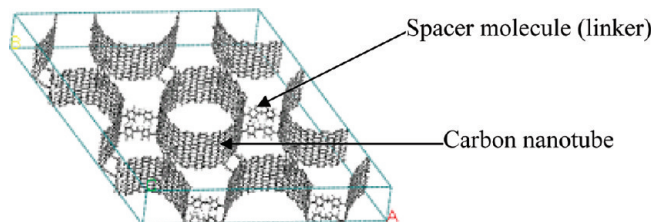


Figure 1. Carbon nanotube scaffold.

A key approach to increase the adsorption capacity of CNTs is by increasing their effective adsorption surface area. After processing, carbon nanotubes usually remain in the form of bundles or ropes made up of several individual nanotubes which are attached to each other by cohesive force.<sup>13–16</sup> As a result, most of the nanotube surfaces remain inaccessible for H<sub>2</sub> molecules. This in turn yields lower H<sub>2</sub> adsorption capacity. If the outer surface areas of all the tubes in the bundles could be exposed to H<sub>2</sub> molecules, then that alone would have improved the adsorption capacity of carbon nanotubes. Various researchers have pointed out this problem and suggested that the intertube distance (or the van der Waals gap) should be increased to increase accessible surface.<sup>15–18</sup> Carbon nanotubes produced via most of the processing techniques are end-capped. To further increase adsorption surface area, these caps may also be removed by special treatment.<sup>16,19</sup>

One way to expose the outer surface areas of carbon nanotubes is to insert spacers between the individual tubes, so that the tubes, instead of forming cohesive bundles, form scaffolding structures as suggested in Figure 1. Covalent functionalizations using different cross-linking agents<sup>14,18,20</sup> may be used as spacers to develop such carbon nanotube scaffolds. These scaffolding structures with their exposed outer tube surface can have higher H<sub>2</sub> adsorption capacity. In fact, Leonard et al.<sup>14</sup> found that the H<sub>2</sub> sorption capacity of a cross-linked single walled carbon nanotube scaffold is almost twice of that of other carbon materials like activated carbon, etc. This is a new approach, and hence not many systematic studies are

\* To whom correspondence should be addressed. E-mail: Tahir.Cagin@chemail.tamu.edu. Phone: (979) 862-1449. Fax: (979) 845-6446.

available to indicate how the sorption capacity depends on the choice of tube diameter, cross-linker (spacer) frequency, and covalent functionalization of tube surface. In addition, the adsorption capacity of CNTs can be improved further by incorporating certain metals like Li, K, and Ti in the tube wall.<sup>21–23</sup> Thus, a similar approach can be also adopted for scaffolded CNT structures to increase their adsorption capacity even further.

This paper presents molecular simulation based analysis of the sorption capacity of single walled carbon nanotube scaffolds. We studied the effect of different tube diameters and cross-linker densities on the adsorption capacity. Experiments indicated that tube chirality does not have significant effect on the sorption capacity and sorption energy;<sup>24</sup> therefore, we have carried out the study with only a single type of tube chirality (armchair type nanotubes) and only a single case of zigzag type nanotube. We prepared scaffolds with (6, 6), (9, 9), (12, 12), (15, 15), and (18, 18) carbon nanotubes with corresponding diameters 8.14, 12.20, 16.27, 20.34, and 24.4 Å, respectively. Our zigzag type tube (21, 0) has similar diameter (16.44 Å) as the (12, 12) nanotube (16.27 Å), making it easier for comparison with at least one case. We observed that as tube diameter increased, sorption capacity also increased. As expected we do not see any significant change in sorption capacity based on chirality.

We also studied adsorption capacity of structures with different cross-linker (spacer) frequencies. A particular cross-linking agent, methylene dianiline, was attached after every 4 (4 L), 7 (7 L), 9 (9 L), and 12 layers (12 L) of benzene rings (on the CNT) so that the linker is placed every 9.8, 17.2, 22.1, and 29.5 Å, respectively, along the axis of the tube. For the (21, 0) zigzag tube, the linkers were placed after every 2 (2 L), 4 (4 L), 5 (5 L), and 7 layers (7 L) so that the linker is placed after 8.52, 17.04, 21.3, and 29.82 Å, respectively, along the length of the tube. This was done to maintain similar spacer distance as in the armchair tubes. We found that sorption capacity increases with linker distance. This particular linker was chosen by Leonard et al.,<sup>14</sup> because it gave sufficient intertube distance of greater than 7–9 Å, which is desirable for molecular hydrogen packing and the necessary rigidity to the structure.<sup>14</sup> As we decided to study effect of linker frequency and tube diameter, we used this same linker as the reference.

Furthermore, we studied the effect of additional functional groups (nitrobenzene, chlorobenzene, carbene, carboxybenzene, aminobenzene, and their sulfonates) on the sorption capacity of the (12, 12) and (18, 18) carbon nanotube based scaffold. We chose these functional groups because they can be attached to the CNTs.<sup>14,18,20</sup> Finally, we decorated (12, 12) and (18, 18) carbon nanotube based scaffolds with Li<sup>+</sup> at a stoichiometry similar to LiC<sub>6</sub> to assess the influence of Li<sup>+</sup> on sorption behavior, because it is known to increase the sorption capacity of CNTs. Although, in our simulations, we do not find any beneficial effect of functional groups on the tube wall, when the (18,18) tube was externally decorated with Li<sup>+</sup> at a stoichiometry similar to LiC<sub>6</sub>, the total sorption capacity of the resulting scaffold was increased to 5.84 wt % at –30 °C (lowest DOE target temperature<sup>3</sup>) at 100 atm compared to 3.72 wt % for bare tubes at 298 K and 100 atm. In addition to analyzing the adsorption behavior in terms of energetics, mass density maps, details of sorption, and sorption kinetics, we have used a theoretical framework addressing the adsorption thermodynamics of all these systems based on isosteric heat. In the next section, we will describe the details of the carbon nanotube

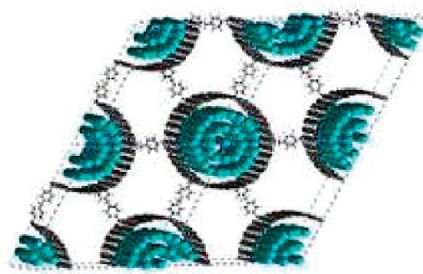


Figure 2. Scaffold with point particles inside the tubes.

structures, simulation models, and analysis methods that were used in this study.

## 2. Simulation Methods

**2.1. Scaffold Structures.** The nanoscaffolds with (6, 6), (9, 9), (12, 12), (21, 0), (15, 15) and (18, 18) tubes, having tube diameters 8.14, 12.20, 16.27, 16.44, 20.34, and 24.4 Å, respectively, were prepared by using the Materials Studio (MS)<sup>25</sup> suite of programs. The tubes were arranged in a triangular lattice, connected by methylene dianiline linker. For a (*n*, *n*) or (*n*, 0) tube, *n* is a multiple of three, because the linkers were placed 120° apart on the circumference of the tube cross section to get a strain-free triangular lattice. The linker length is ~11 Å, and this effectively defines the distance between the tubes. For each type of tube, different structures were prepared with linker molecule attached at different spacings in the tube axis direction for studies aiming to understanding the role of linker spacing/frequency on the sorption behavior. Scaffolds with linker spacings of 4, 7, 9, and 12 L, having interlinker distances of 9.8, 17.2, 22.1, and 29.5 Å, respectively, were considered.

**2.2. Sorption Simulations.** The sorption studies were performed by grand canonical Monte Carlo (GCMC) simulation using Cerius2 software.<sup>26</sup> We choose the GCMC method because it is computationally inexpensive and a quick yet reliable method to get a general idea about the hydrogen sorption efficiency of nanoporous materials based on van der Waals and electrostatic interactions. In this method, the H<sub>2</sub> sorbate molecules (with rotational and translation degrees of freedom) are randomly created and destroyed. Probability of creation and destruction of hydrogen molecules was set at 0.3. Dreiding force field, which is suitable for organic molecules, was used to perform the simulations. For proper electrostatic interaction representation, hydrogen was specifically modeled as a quadrupole with –0.96e charge at the center and +0.48e charge positioned at the two ends. In all these simulations, Coulomb interactions were considered in addition to van der Waals interactions, while calculating the total interaction energy and forces. Special attention was given to exclude the spaces that are inaccessible to the sorbate molecules. Atoms in the scaffold framework were kept rigid during the simulation.

Usually when the tubes are prepared experimentally, they are capped at both ends by fullerene which prevents hydrogen sorption inside the tubes. To simulate this, we placed a suitable diameter column of point particles inside the nanotubes, which blocked hydrogen sorption on the inside tube surfaces (shown as blue spheres in Figure 2).

The simulations were run for 1 million steps at each pressure, of which the last half a million steps were considered for data collection. Each simulation was started at the lowest pressure with an empty framework. Each subsequent simulation step was started with the final structure of the previous step. Simulations were carried out at two different temperatures: 77 and 298 K,

over a range of gas pressures (1–100 atm). Surface area and accessible volumes were calculated by using the method provided in the Cerius2 program.

Cerius2 uses the Connolly surface area method to find the solvent accessible surface of a molecule or a structure. The Connolly surface is the van der Waals (VDW) surface that is available to a probe molecule having a nonzero radius. A spherical probe (in this case a molecule with radius 1.4 Å) is rolled on the VDW surface of the scaffold structure to generate the Connolly surface. This gives the surface area available for sorption.

In our simulation we have assumed that the same periodic boundary condition exists in all direction. This means that all the cells are equally available for gas adsorption. In real structures, the spacer material creates a barrier for hydrogen flow that has to diffuse in the cells that are embedded deep inside the scaffold. Our simulation does not capture the hydrogen diffusion barrier due to the depth of the scaffold material which will lower the adsorption capacity in the cells that are buried deep inside. We only observe that the effect of denser spacer arrangement on sorption capacity is due to steric hindrance to gas diffusion, but not due to depth of scaffold material.

### 2.3. Studies with Functionalization on Tube Surface.

Based on the initial simulation results with scaffolds with different tube diameters, the best performing scaffold made up of (18, 18) tubes was selected for further studies. Also considering the fact that experimentally observed tube diameter is  $\sim 14$  Å, the scaffold with (12, 12) tube having similar 16.27 Å diameter was also chosen to be studied further. These (12, 12) and (18, 18) tube scaffolds were used to study effect of exclusion of tube interiors, different covalent functionalization, and Li incorporation.

To study the effect of a variety of functionalization of the tube surfaces on sorption capacity in the similar lines as Leonard et al.,<sup>14</sup> who studied with only the chlorobenzene group, we have added the following: chlorobenzene, nitro, carboxy, amino, and carbene functional groups with and without sulfonate groups. These functional groups were attached to the tube exterior walls, in addition to the cross-linking agent.

**2.4. Studies with Li.** For studying the effect of Li incorporation on tube surfaces, we incorporated 100, 120, and 150 Li<sup>+</sup> atoms on the external surface of (12, 12), 12 L and (18, 18), 12 L tube scaffolds. These values were chosen considering the fact that previously studied<sup>21,22</sup> optimum Li:C ratio was found to be 1:6. The force field was set with Lennard-Jones (L-J) 12–6 potential parameters of Li. These parameters were based on the experimental LiF crystal properties. The experimental cohesive energy and lattice parameter of LiF crystal is 246 kcal/mol and 4.02 Å.<sup>27</sup> The LJ parameters  $r_0$  and  $D_0$  for Li as given in the Dreiding force field were optimized until a matching value (within  $\pm 5\%$  of the experimental value) for the cohesive energy and the lattice parameters was obtained. The final LJ parameters for Li are  $r_0 = 2.6975$  Å and  $D_0 = 0.065$  kcal/mol. This type of parametrization has been done for other metals like K, Rb, and Br<sub>2</sub>, and they were found to be good at predicting various properties for metal intercalated graphite intercalation compound.<sup>28</sup> Thus we assumed that this parametrization method is also good at capturing Li interaction with CNT and hydrogen, and therefore it was used in our simulation.

**2.5. Sorption Capacity Measurement.** Sorption capacity was measured in terms of total adsorption and excess adsorption percentages.

**TABLE 1: Physical Properties of Nanotube Scaffolds Prepared for the Simulations**

tube type ( <i>n</i> , <i>n</i> ) diameter	functionalization	cross- linking periodicity (Å)	density (g/cc)	surface area (m <sup>2</sup> /g)
(6, 6) 8.14 Å	4 L	9.83	0.809448	2781.513
	7 L	17.23	0.712581	2553.158
	9 L	22.15	0.67953	2473.886
	12 L	29.52	0.649885	2385.137
(9, 9) 12.20 Å	4 L	9.83	0.739811	2188.441
	7 L	17.23	0.679319	2539.790
	9 L	22.15	0.662859	2475.454
	12 L	29.52	0.631833	2421.857
(12, 12) 16.27 Å	4 L	9.83	0.678073	2666.411
	7 L	17.23	0.627196	2523.567
	9 L	22.15	0.614861	2479.290
	12 L	29.52	0.598775	2454.506
	12 L (6chloro)	29.52	0.656707	2615.505
	12 L (18chloro)	29.52	0.769751	2768.567
	12 L (6cl4sulfo)	29.52	0.719278	2647.463
	12 L	29.52	0.598775	1476.017
	(only outer surface)			
	4 L	9.83	0.627025	2605.198
(15, 15) 20.34 Å	7 L	17.23	0.585594	2454.279
	9 L	22.15	0.571777	2425.953
	12 L	29.52	0.561984	2414.323
	4 L	9.83	0.575879	2551.447
(18, 18) 24.4 Å	7 L	17.23	0.544859	2438.269
	9 L	22.15	0.536811	2404.194
	12 L	29.52	0.525671	2383.982
	12 L (6chloro)	29.52	0.55712	2517.512
	12 L (6cl4sulfo)	29.52	0.596679	2596.863
	12 L	29.52	0.525671	1368.341
	(only outer surface)			
(21, 0) 16.44 Å	2 L	8.52	0.6966	2573.634
	4 L	17.04	0.629818	2346.271
	5 L	21.3	0.616624	2299.179
	7 L	29.82	0.594123	2248.593

The total adsorption capacity % is defined as

$$\text{total wt \%} = \frac{N^*m}{(M + N^*m)} * 100$$

where  $N$  is the total loading of hydrogen (number of molecules),  $m$  is the molecular weight of H<sub>2</sub>, and  $M$  is the molecular weight of the empty scaffold framework.

Excess adsorption is defined as the amount of additional hydrogen that can be stored in a given volume when adsorbing substrate is present, compared to free volume hydrogen storage. A positive excess capacity measures the effectiveness of the adsorbing substrate. Therefore the excess adsorption capacity % is defined as

$$\text{excess wt \%} = \frac{(N - \rho_{\text{bulk}} V_{\text{cell}}) * m}{\{M + (N - \rho_{\text{bulk}} V_{\text{cell}}) * m\}} * 100$$

where  $\rho_{\text{bulk}}$  is the bulk hydrogen density (molecules per m<sup>3</sup>) at the same temperature and pressure at which the adsorption took place. Hydrogen density was obtained from the NIST database.<sup>29</sup>

## 3. Results and Discussion

**3.1. Physical Properties of the Scaffoldings.** The key physical properties like surface area, volume, and density, which affect the sorption capacity of the SWNT scaffolds, are given in Table 1.

We prepared several different types of scaffolds with different tube diameter, linker periodicity, and tube surface functionalization for this study. The specific surface areas of the scaffolds



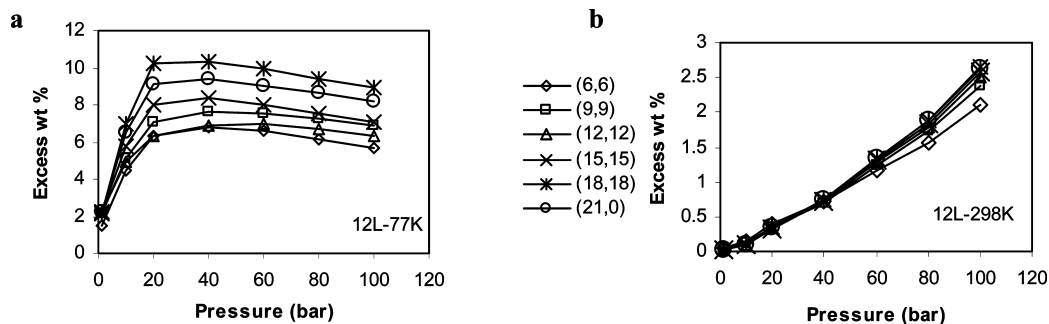


Figure 3. Excess sorption capacity variation with pressure at two different temperatures.

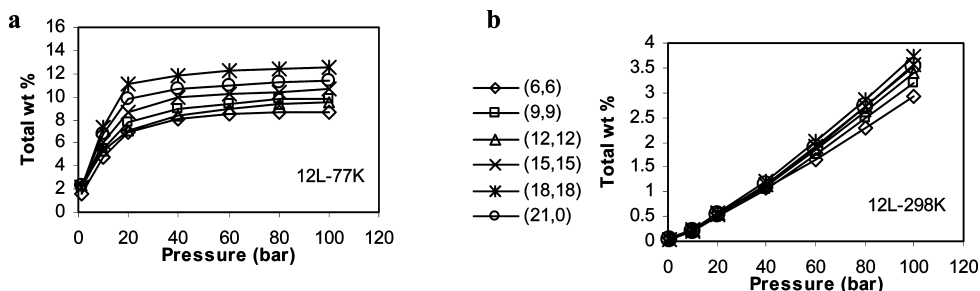


Figure 4. Total sorption capacity variation with pressure at two different temperatures.

vary between 1368 and 2781 m<sup>2</sup>/g, which are comparable to the surface areas of typical carbon materials.<sup>5,16</sup> But the estimates from our simulation are higher than the experimental estimates of Leonard et al.<sup>14</sup> For example, the densities of these scaffolds vary from 0.52 to 0.8 g/cm<sup>3</sup>, which is lower than the experimentally observed densities (1.0–1.2 g/cm<sup>3</sup>) for SWCNT scaffolds.<sup>14</sup> Their experimentally observed surface area of 515 m<sup>2</sup>/g is less compared to the 1368–2781 m<sup>2</sup>/g values obtained from our simulation. Leonard et al.<sup>14</sup> used oleum (fuming sulfuric acid) in the preparation process. Oleum tends to attach to the linkers and tube wall, and the researchers have to employ various strategies, such as heating at high temperature, reducing the number of linkers, etc., to remove the solvent molecule. In addition water as contaminant may be present,<sup>30</sup> which can lead to less than ideal surface area estimates. These issues are often associated with experimental work.

However, in our case we worked with atomically clean structures without any defects, imperfections, or impurities, which gave us the ideal surface area estimate based on theoretical Connolly surface area calculation. Therefore, given these realities we speculated that the presence of solvent, catalyst, water, impurities, etc., might be some reasons which might explain the discrepancy between calculated (larger value) and experimental (lower values) surface areas.

**3.2. Sorption Capacity Variation with Gas Pressure.** Grand canonical Monte Carlo (GCMC) simulations were performed on the scaffolds at pressures in the range of 1–100 bar at two temperatures, 298 and 77 K. Figures 3 and 4 present the adsorption isotherms, both in terms of excess adsorption capacity and total capacity, respectively, for the scaffolds with linker periodicity 12 L (cross-linkers at every 12th layer). This linker separation exhibited the highest sorption capacity. At both temperatures, the scaffold of (18, 18) SWNTs with cross-linkers at 12 L exhibited the highest sorption capacity. For all types of scaffolds, the excess adsorption capacity at 77 K is higher than that at 298 K. This is because, at low temperature, repulsive interactions between hydrogen molecules are less compared to those at higher temperature;<sup>2</sup> thus, more hydrogen molecules can be packed together.

The 77 K sorption isotherms in Figure 4a show that the capacity reached a saturation point around the 20–40 bar pressure region and only increased slightly at higher pressures above 40 bar. In Figure 3a, in this saturation region the excess capacity dropped slightly because the bulk density of hydrogen  $\rho_{\text{bulk}}$  increased more rapidly than the total loading of adsorbed hydrogen  $N$  (refer to the equation for calculating excess adsorption in section 2) and not because the adsorption decreased.

The (18,18), 12 L scaffold showed the highest excess sorption capacity of 10.33 wt % (11.87% total capacity) at 77 K and 40 bar. The maximum total capacity was 12.58 wt % with the (18, 18), 12 L scaffold, obtained at 77 K and 100 bar. The volumetric sorption capacity (not shown in the figure) reached a maximum value of 81 g/L for the (12, 12) tube with cross-linker with 9 L periodicity at 77 K, 100 atm. At 77 K the volumetric capacity for all other scaffolds, except the (9, 9) tube with cross-linkers at 4 L, exceeded the DOE volumetric storage target (45 g/L).<sup>3</sup>

At 298 K, for a pressure range up to 40 bar, there is not much difference in sorption capacity between the scaffolds of different tubes (Figures 3b and 4b). The difference becomes prominent only at higher pressure. At 298 K, the (18, 18) tube with 12 L cross-linker spacing exhibited a maximum excess capacity of 2.66 wt % (total capacity 3.72 wt %) at 100 bar without reaching saturation. This indicates that there is still plenty of space available for further storage at 298 K, which may be achieved at higher pressure. The (12, 12), 9 L scaffold has the highest volumetric capacity of 28 g/L at 298 K among all.

The sorption capacity did not vary much with tube chirality at 298 K. Sorption capacity of the (12, 12) tube at 100 atm, 298 K was 3.39 total wt % compared to 3.51 total wt % for the (21, 0) tube under similar conditions. However, at 77 K, the (21, 0) tube adsorbed a higher amount compared to the (12, 12) tube having similar diameter and cross-linker distance. For example, the (12, 12) tube adsorbs 8.29 total wt % at 40 atm, 77 K compared to 10.67 total wt % for the (21, 0) tube under similar conditions. This difference becomes higher at high pressure. At 100 atm, the 77 K (12, 12) tube adsorbs 9.57 total

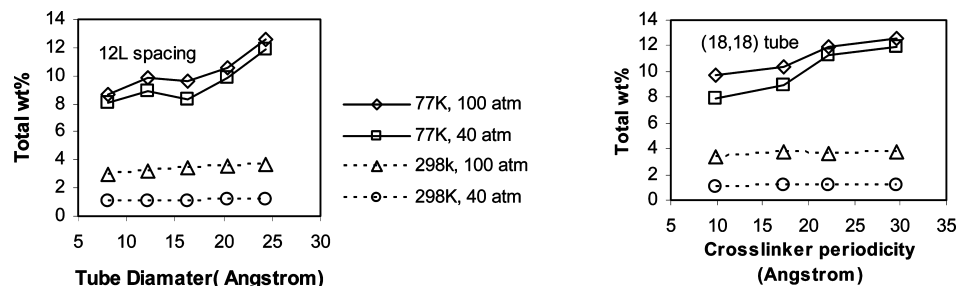


Figure 5. Sorption capacity variation with tube diameter and interlinker distance.

wt % compared to 11.32 total wt % for the (21, 0) tube under similar conditions. Thus, it seems tube chirality may have some effect at lower temperature but does not seem important at higher temperature. However, the specific reason for this difference needs further investigation.

The higher sorption capacity at 77 K corroborates with figures reported by other researchers.<sup>16,17</sup> Darkrim and Levesque<sup>17</sup> reported a total capacity of 11.2 wt % at 10 MPa (100 bar), 77 K with tube diameter 22 Å and intertube spacing of 11 Å. The tube diameter and spacing reported by Darkrim and Levesque are quite similar to our 24 Å tube diameter and 11 Å tube spacing of the (18, 18) tube scaffold. Their reported adsorption capacities also agree with our values.

**3.3. Impact of Tube Diameter and Linker Spacing on Sorption Capacity.** Figure 5 summarizes the results presented in Figure 4 and shows that tube increasing diameter and linker spacing improve sorption capacity at higher pressures. These observations are explained as follows. For smaller diameter tubes, the van der Waals potential from opposite tube inner surface walls overlaps to create an energetically favorable location. However, narrow tubes only allow a very thin column of sorbate molecules inside the tubes. However, larger diameter tubes allow a much thicker layer of hydrogen molecules, even though these interaction sites have lower energy compared to narrower tubes (illustrated in section 3.6). Thus, larger availability of free space volume within the large diameter tubes favors adsorption capacity at higher pressure (loading).

Similarly higher linker frequency also reduces the available volume within the confines of the outer surface of the tubes and the linkers. This is because each linker occupies space and higher linker frequency (and lower interlinker distance) leaves smaller volume for the adsorption and reduces hydrogen diffusion due to steric hindrance. Therefore, it seems that adsorption capacity increases with free space volume within the scaffolds. We call these “volume effects”.

**3.4. Sorption Capacity of Capped Tube.** Carbon nanotubes that are produced in laboratories in normal production process are generally capped at the ends. This means the inner tube surfaces are not accessible to sorbate molecules unless these tubes are uncapped by special treatment. Such exclusion of the interior of tubes reduces the sorption capacity by almost half. For example, the excess capacity for the open (18, 18) tube is 10.33 wt % at 77 K at 40 atm, whereas it is only 6.30 wt % for the tubes when the interior volume is prohibited under the same loading conditions. This difference is more pronounced for larger (18, 18) tube scaffold compared to the (12, 12) tube scaffold. This is because a large diameter tube allows a larger surface inside the tubes compared to the space outside the tubes. Therefore, for large tubes when sorption inside the tubes is excluded, the sorption capacity reduces more pronouncedly from that of the uncapped tubes. The interior volume is also larger for bigger diameter tubes. This means two things. First, the inner

free volume is an important factor toward higher sorption capacity. Second, to have high sorption capacity open tube scaffolds are necessary. Thus all other simulations and analysis were conducted with the open tube scaffold models.

**3.5. Thermodynamics of Adsorption: Isosteric Heat.** When a gas molecule is adsorbed on the surface, some amount of heat is released. This is called isosteric heat of adsorption ( $q_{st}$ ). This is a measure of the strength of the interaction between sorbate and sorbent/substrate molecules. Therefore a higher isosteric heat indicates a stronger van der Waals interaction between the sorbate and surface molecules, and therefore a greater adsorption capacity. Isosteric heat influences adsorption equilibria, kinetics, and overall sorption process.<sup>31</sup> Thus, it is important to study variation of  $q_{st}$ . The computed values of  $q_{st}$  for these scaffolds lie in the range of 0.88–2.14 kcal/mol. These values are comparable with reported values for other carbonaceous materials.<sup>16,24</sup>

Sircar and Cao<sup>31</sup> have explained the sorption dynamics to clarify how isosteric heat varies with loading (hydrogen sorption). Isosteric heat may vary in a different manner depending on the nature of interaction. These phenomena can be classified as follows:

1. A constant  $q_{st}$  with increasing loading shows absence of sorbet–sorbet interaction, so that the  $q_{st}$  does not change even though more sorbate molecules are added. This also shows that the substrate is energetically homogeneous, which means there are no special locations on the substrate surfaces that have higher  $q_{st}$  to encourage preferential adsorption.

2. An increase in  $q_{st}$  with loading indicates sorbet–sorbet van der Waals interaction (at the attractive range) at high loading.<sup>31</sup>

3. A gradual decrease in  $q_{st}$  with loading happens due to energetic heterogeneity of the surface. Once all the adsorption locations on the substrate which has higher  $q_{st}$  get filled up, then only low  $q_{st}$  sites are available for further loading, showing a falling  $q_{st}$  trend.

4. Another case may be an initial increase followed by a decrease in  $q_{st}$  with increasing loading. In this case,  $q_{st}$  initially increases due to sorbet–sorbet van der Waals interaction (when within the attractive range), but as more sorbate is added to the system under high pressure and temperature, sorbate–sorbate repulsion comes into play to deteriorate the adsorption phenomenon.

All these phenomena were observed in our sorption studies. Behavior of  $q_{st}$  with various loadings for the ( $n$ ,  $n$ ) and (21, 0) tubes with the same 12 L cross-linker spacing at 298 K is shown in Figure 6.

As observed in Figure 6,  $q_{st}$  is almost constant at different loading for all the scaffolds except for the (6, 6) nanotube based one. For the (6, 6) tube scaffold, at low loading, the initial  $q_{st}$  is quite high, and it decreases with loading up to a certain point. Later, as loading increases, the  $q_{st}$  becomes flat similar to the

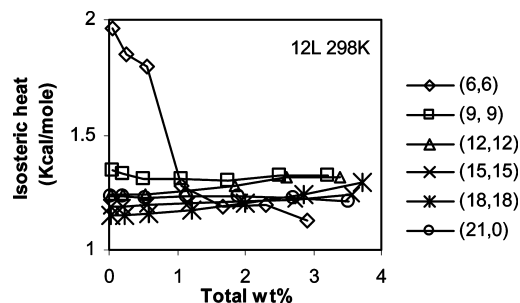


Figure 6. Variation of isosteric heat with total wt % at 298 K.

behavior observed for other tubes. This observation is explained as follows. For the (6, 6) tube, the tube diameter is small, and thus, as explained before, this leads to superposition of the attractive van der Waals interactions from both sides of the tube wall on the hydrogen molecules in the proximity of tube surfaces. For these adsorption sites the sorbent–substrate interaction potential is strong, which results in a high  $q_{st}$ . At low gas pressure or low loading, this tube wall potential dominates,<sup>15</sup> because sorbent molecules first get adsorbed in these sites. As loading increases, all these sites get filled up, and the sorbent molecules then get accommodated to outer surface adsorption sites, where the potential field is weak and  $q_{st}$  is uniformly low.

In the case of other armchair tubes and the zigzag tube (21, 0), the  $q_{st}$  trend remains flat with increased loading. This indicates an energetically homogeneous substrate and absence of sorbate–sorbate interaction. At 298 K since the loading is still low compared to saturation loading, the gas molecules are farther apart and are not interacting with each other, showing no change in  $q_{st}$ .

Figure 7a shows that at low (1 atm) pressure, as the tube diameter increases, the  $q_{st}$  decreases. For every point in the inner surface of the tube, there is an overlap of potential from other neighboring points on the inner tube surface. This curvature effect is greater for higher curvature tubes (smaller diameter means greater curvature).<sup>32</sup> For the outer tube surface, an opposite kind of curvature effect is manifested because the potential overlap decreases with increased curvature (smaller diameters). Both curvature effects are evident only at lower pressures. At higher pressures, other effects (e.g., volume effect) dominate to increase the adsorption capacity as the tube diameter increases. However, the isosteric heat does not change much with linker periodicity as expected (Figure 7b), because linkers do not create a large number of high interaction sites. This will be evident in the next section.

Behavior of the isosteric heat for the scaffolds at 77 K is presented in Figure 8. The curves do not display a consistent pattern or trend. In the case of (6, 6) tubes,  $q_{st}$  initially decreases with loading and then increases. This indicates a three stage sorption loading phenomenon. These three stages are (1) initial adsorption at the higher energy adsorption sites possibly at the inner tube surfaces, (2) followed by adsorption at the next available sites that have low adsorption energy which shows decrease in  $q_{st}$ , and (3) last, as all the sites get populated with more and more sorbate molecules under higher pressure, there are higher sorbate–sorbate interactions which increase  $q_{st}$ .

For (12, 12) tubes,  $q_{st}$  gradually decreases with increase of loading. This type of trend indicates an energetically heterogeneous surface; i.e., higher energy sites get populated first followed by lower energy sites. However, for (18, 18) and (21, 0) tubes,  $q_{st}$  increases with loading indicating sorbate–sorbate interactions at high loading. This result also shows a difference

in trend for tubes with different chirality, such as (12, 12) and (21, 0) tubes having similar diameter and cross-linker spacing. It may be recalled that at 77 K, the (21, 0) tube has higher sorption capacity compared to the (12, 12) tube although they have similar diameter and linker spacing. This higher capacity may have contributed to sorbate–sorbate lateral interaction and thus high isosteric heat for the (21, 0) tube.

Figure 9a shows variations of  $q_{st}$  with diameter. The trend is the same as in the case of 298 K due to similar reasons as explained earlier. Similarly, the isosteric heat also remains flat with variation in linker periodicity (Figure 9b).

**3.6. Physical Distribution of Adsorbates.** The mass density plot and snapshot of physical distribution of hydrogen adsorbate inside the scaffolds confirm the insights presented in the previous section. Figures 10 and 11 show the mass density plots of hydrogen adsorbate molecules superimposed on the scaffold structures. A mass density plot gives the position of center of mass of each sorbate molecule in the framework as their positions were sampled. The red dots represent the high interaction (higher  $q_{st}$ ) zones, while the blue dots represent low interaction areas, and yellow through green zones have intermediate  $q_{st}$  values. The high interaction sites have higher preference for adsorption and are occupied first.

Figures 10a and 10b show the top view and side view of the mass density plot in the case of (6, 6), 12 L scaffold at 77 K, 1 atm. Figure 10c shows the side view of the empty (6, 6), 12 L scaffold structure to help interpret the side view shown in Figure 10b. Figure 11 shows the top view of the H<sub>2</sub> mass density plot for the (18, 18) 12 L scaffold at the same temperature and pressure. There are several observations to be made from these figures. From Figures 10a and 10b, it is evident that the adsorption location of hydrogen molecules inside the (6, 6) tube is confined to a very narrow column (red and yellow color). This column is shown as a small red circle in the top view (Figure 10a) and a red–yellow elongated tube from the side view (Figure 10b). For bigger diameter scaffold, for example in (18, 18), this column is much thicker (bigger red–yellow circles in Figure 11). This shows that bigger diameter tubes allow larger adsorption volume (i.e., the volume effect) as mentioned in section 3.3.

The red, yellow, and dense green marked locations in Figures 10a, 10b, and 11 show the high energy interaction sites in the immediate vicinity of (1) inner and (2) outer tube surfaces, (3) near the locations where the linkers are attached on tube external surfaces, and (4) all around the linkers. The dark locations show the volumes where there are no adsorption sites. These are generally the spaces which are taken up by the carbon atoms and linker molecules. It is evident from Figure 10b that linkers create only a small amount of high interaction sites compared to the tube surfaces. It is also evident from Figure 10b that the linkers take up significant space, which means that the larger linker densities (smaller interlinker distances) will leave lesser space for the adsorption locations and will cause lower adsorption as mentioned in section 3.3.

**3.7. Sorption Capacity, Surface Area, and Interlinker Distance.** As adsorption is a surface phenomenon, it is naturally expected that the adsorption capacity should increase with surface area. With such expectations, researchers like Cahine et al.<sup>33</sup> suggested that typical activated carbon materials achieve ~1 wt % for every 500 m<sup>2</sup>/g for a pressure range of 30–50 atm. For CNT scaffolds, Leonard et al.<sup>14</sup> suggested a capacity of 3.7 wt % for 1000 m<sup>2</sup>/g at 77 K at 2 bar. For comparison, here we present the sorption capacities and specific surface areas for different scaffolds at 1 and 40 atm for 77 and 298 K.



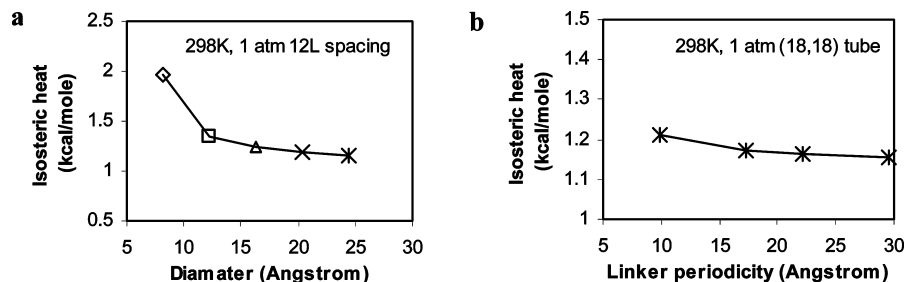


**Figure 7.** Variation of isosteric heat with (a) tube diameter and (b) interlinker distance at 298 K.

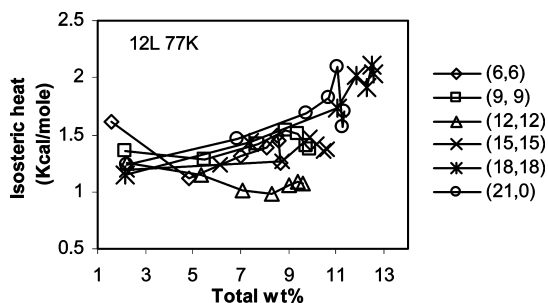


**Figure 8.** Variation of isosteric heat with total wt % at 77 K.

However, in real scaffolds, some other factors may come into play to conceal a positive correlation between surface area and adsorption capacity.

The open tube scaffolds have surface areas in the range of 2188–2781 m<sup>2</sup>/g. Total sorption capacities of these scaffolds at 77 K, 1 atm are in the range of 1.22–2.44 wt %. At 298 K, 1 atm these numbers are between 0.018 and 0.06 wt %, at 77 K, 40 atm they are between 5.01 and 11.86 wt %, and at 298 K, 40 atm the values are within 0.77–1.21 wt %. For the (18, 18) tube scaffold, where the sorption to interior regions is prohibited, the surface area was around 1500 m<sup>2</sup>/g, and this scaffold showed a total sorption capacity of 1.22 wt % at 77 K, 1 atm. This is less than the capacity suggested by Leonard et al.<sup>14</sup> (~3.7 wt % for 1000 m<sup>2</sup>/g at 77 K, 2 atm). A higher capacity is observed in their experiments compared to our simulations. This is perhaps due to the influence of impurities present in the experimental samples. In comparison, our simulations consider pristine structures and ideal behaviors.

To show the relationship between sorption, surface area, and cross-linker periodicity of open tubes scaffolds, these metrics are presented in Figure 12.

From Figure 12, we make the following key observations. First, in general, the smaller tube scaffolds show lower capacity than others because the smaller tubes allow only a limited amount of sorbate molecules within the tubes due to limited tube volume (the volume effect).

The second observation is that at lower (1 atm) pressure the sorption capacities increase with increase of specific surface areas, but the opposite is true at higher (40 atm) pressure. It seems that availability of more surface area favors sorption capacity at lower pressure ranges (e.g., at 1 atm), but other factor(s) dominate at higher pressure ranges (e.g., 40 atm). The volume effect and steric hindrances, as elucidated in section 3.3, can explain why capacity and surface areas are negatively correlated at high pressure. Higher linker frequency decreases free volume and increases steric hindrance. On the other hand, higher linker frequency (with lower interlinker distance) scaffolds have higher specific surface area (Table 1 in section 3.1). Therefore, it is only natural that sorption capacity and specific surface areas will be negatively correlated.

**3.8. Effect of Different Functional Group.** Covalent functionalization of tube surfaces in SWNTs by using aryl diazonium chemistry leads to various beneficial properties.<sup>24</sup> For example, the isosteric heat may be manipulated by attaching functional groups. Leonard et al.<sup>14</sup> attached chlorobenzene to the tube wall to create space between the tubes and keep them separated, while reducing linker density (which improves the volume effect). With this approach they reported an increase in porosity and sorption capacity. Thus, we were motivated to assess the real benefits of tube surface functionalization on sorption capacity. This is because we suspect that other factors might have contributed to the increase in sorption, rather than the tube surface functionalization alone. Leonard et al.<sup>14</sup> used sulfuric acid (oleum) in the preparation process; hence, there is a possibility that some sulfonate groups may be present in the tubes which improved sorption capacity. This hypothesis is supported by a report on the beneficial effect of sulfonate group on gas storage capacity.<sup>34</sup>

To assess the benefits of functionalization, we attached various kinds of groups on the tube outer surface and assessed their effect on sorption capacity. At this point onward, we choose to study only the (12, 12), and (18, 18) tube scaffolds for the reasons stated earlier in section 2.3.

Figure 13a gives the schematic representation of various functional groups used in our study, and Figure 13b displays a scaffold model where additional functionality is present.

Figure 14 presents the adsorption capacities of these scaffolds for various pressures at 77 and 298 K temperatures. We observed that with the incorporation of different functional groups, both volumetric adsorption and the total adsorption capacity wt % decreased. Although the presence of additional function groups increases the surface area, they reduce the available volume of the scaffolds and thus reduce sorption capacity.

The presence of functional groups does impart some charges to the tube walls and improves isosteric heat; however, this charge is very small. This is not sufficient to compensate for the steric hindrance induced loss in volume due to the presence of the functional groups on the tube walls. Thus, we contend that the experimental observations of sorption capacity increase by functionalization are primarily due to physical separation created by the functional groups and perhaps also due to residual sulfonates.

**3.9. Impact of Li<sup>+</sup> on the Tube Wall.** Li incorporation on carbon materials improved their hydrogen sorption capacity.<sup>21–23</sup> Li improves sorption capacity by imparting charge to the tubes and thus increases the interaction energy. To study this behavior on scaffolds, we performed simulations with 100, 120, 150 Li<sup>+</sup> ions per unit cell, placed on the outer side of the tube walls for (12, 12) and (18, 18) tube scaffolds where the amounts have a Li:C ratio similar to 1:9, 1:7.5, and 1:6.

Figure 15 shows the space-filling model of Li decorated (18, 18) tube scaffold. Here, the Li<sup>+</sup> are the pink colored spheres.

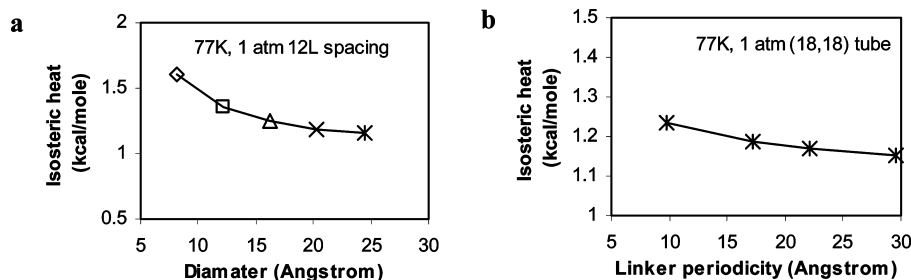


Figure 9. Variation of isosteric heat with tube (a) diameter and (b) interlinker distance at 77 K.

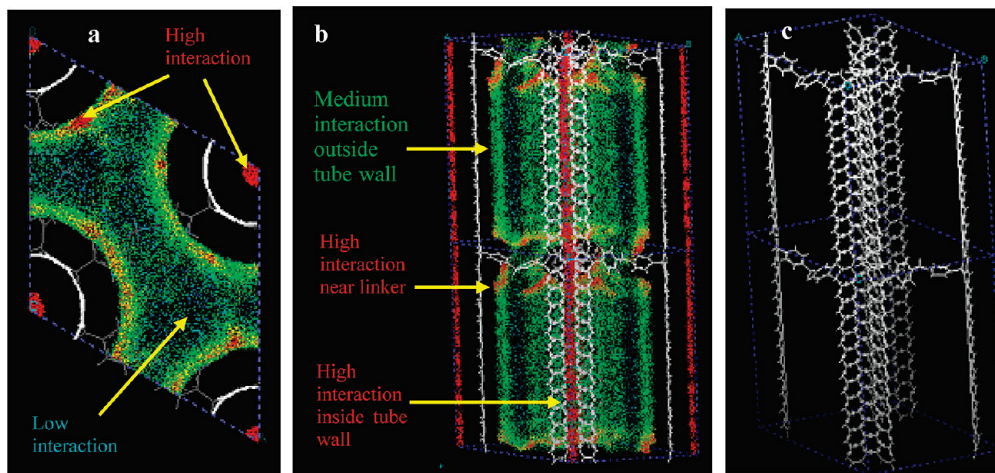


Figure 10. Distribution of hydrogen molecules in the (6, 6) 12 L at 1 atm, 77 K: (a) top view, (b) side view, and (c) bare scaffold.

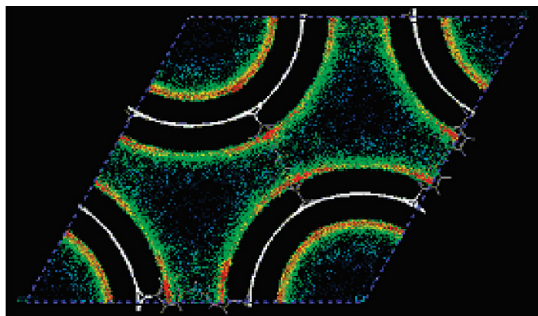


Figure 11. Mass distribution of hydrogen molecules in the (18, 18) 12 L scaffold at 1 atm.

After energy minimization,  $\text{Li}^+$  have almost vertical alignment along the tube wall. As the number of Li increases, the compensating charge on the tube also increases (becomes more negative). For example, 150  $\text{Li}^+$  decorated tubes carry  $\sim -0.1625e$  charge, 100  $\text{Li}^+$  decorated tubes carry  $\sim -0.1094e$  charge compared to the  $\sim -0.0012e$  charge when no  $\text{Li}^+$  is present. The presence of  $\text{Li}^+$  has two different impacts. The presence of  $\text{Li}^+$  increases the van der Waals interaction. In addition, the static charges result in preferable strongly binding Columbic interactions between tube and sorbate molecules;<sup>35</sup> i.e., quadruple moment of hydrogen molecule—negatively charged tube—atoms interactions are very effective in attracting more hydrogen.<sup>35</sup> Both these effects increase the interaction energy  $q_{\text{st}}$  to increase the adsorption and form more dense sorbate layers around the scaffold.

Increase in interaction energy is evident from the mass density plots displayed in Figure 16 which compares hydrogen molecule densities around the (18, 18), 12 L scaffolds with and without the decorating Li atoms. Figure 16a is for the scaffold without Li at 77 K, 1 atm, and Figure 16b is with Li at the same temperature and pressure. Figure 16c is without Li at 298 K, 1

atm, and Figure 16d is with Li at the same condition. Figure 16b and 16d show that when Li atoms are present on the tube outer surface, there is a thicker high interaction zone, shown in red color, near the Li atoms.

Figure 17 shows the impact of  $\text{Li}^+$  on sorption capacity by comparing sorption capacities for scaffolds with and without  $\text{Li}^+$ . Figure 17a shows that the scaffolds with  $\text{Li}^+$  have higher total capacity at 77 K at the lower pressure range (below 6 atm), but a lower capacity at higher pressure range (above 6 atm). The volumetric capacities (not shown in the figure) also show the same pattern. This is because incorporation of Li reduces the available volume but increases interaction potential and surface area. At lower pressures, when the volume effects do not dominate, the higher surface area leads to higher capacity. At higher pressures, when the volume effect dominates, the capacity suffers when Li is present. This is because the molecular weight  $M$  of the Li decorated substrate has increased significantly lowering the excess adsorption capacity wt % ratio.

Figure 17b shows that at 298 K, Li incorporation substantially improved the adsorption capacities. The scaffold with Li decorated (12, 12) tubes shows less capacity than that for the (18, 18) tube.

We found that the optimum Li:C ratio was 1:6 (i.e., 150 Li atoms per cell). At 298 K, the 150  $\text{Li}^+$  atom decorated tube achieved excess capacity 3.39 wt % (total capacity 4.26 wt %) at 100 atm with  $q_{\text{st}}$  being 1.77 kcal/mol compared to bare tube excess capacity of 2.99 wt % (total capacity 4.04 wt %) and  $q_{\text{st}}$  of 1.258 kcal/mol at the same condition. The  $q_{\text{st}}$  of the 150 Li decorated tube at 77 K, 1 atm is 2.68 kcal/mol (11.213 kJ/mol) and at 298 K, 1 atm it is 1.98 kcal/mol (8.29 kJ/mol) compared to the 1.18 kcal/mol (4.93 kJ/mol) for the bare tube at both of these conditions. These values of  $q_{\text{st}}$  of Li decorated tubes and also empty tubes corroborates well with other reported values. For example, for a MOF system,<sup>36</sup> the Li—H binding energy



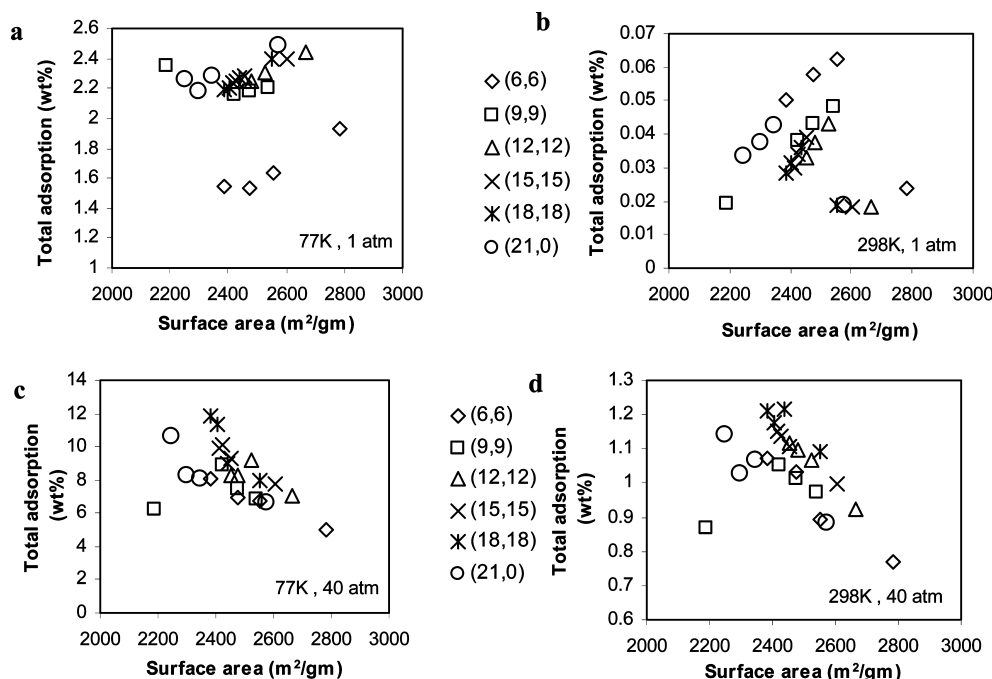


Figure 12. Sorption capacity vs specific surface area at 77 K, 298 K and 1 atm, 40 atm.

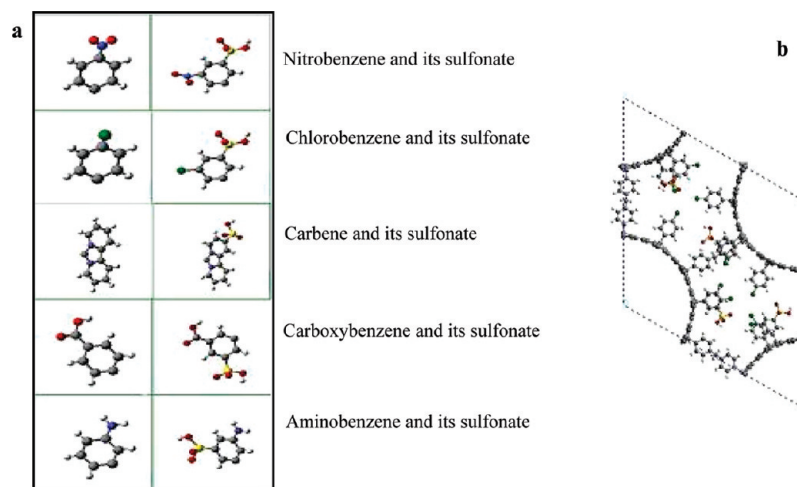


Figure 13. (a) Functional groups that were added to the tube outer surfaces tubes. (b) (18, 18) scaffold showing positions of sulfo-chlorobenzene functional group.

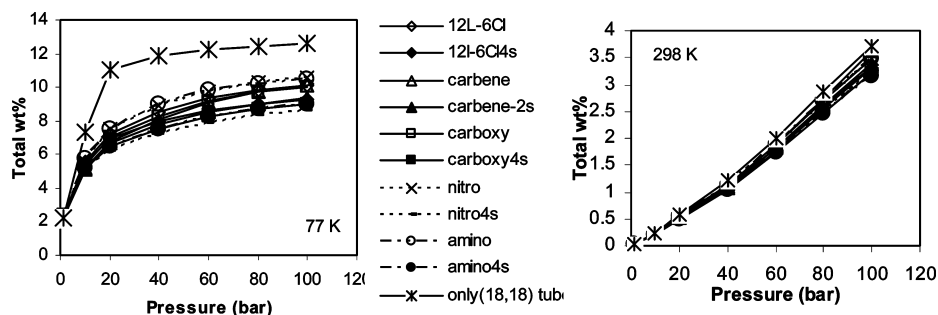
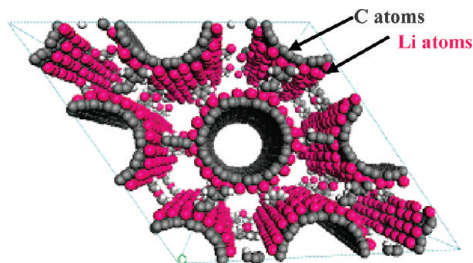


Figure 14. Effect of covalent functionality on sorption capacity of the (18, 18), 12 L scaffold.

was found to be in the range of 12–18 kJ/mol, and for a Li decorated graphene sheet,<sup>37</sup> the binding energy was  $\sim 13$  kJ/mol. The hydrogen binding energy on a simple benzene molecule or graphene sheet is on the order of  $\sim 5$  kJ/mol.<sup>36,37</sup> These values are similar to our calculated values.

The behavior of the isosteric heat curve against excess weight percent for Li decorated scaffolds (Figure 18) show two distinct

patterns at two different temperatures: 77 and 298 K. At 77 K, when Li is present,  $q_{st}$  decreases sharply with increase in loading, whereas for the bare tube without Li, the  $q_{st}$  increases with gas loading. Li creates a very high interaction potential near the tube wall; thus, at low loading (and low pressure), the sorption capacity and  $q_{st}$  both are twice as big compared to the values for bare tubes. This drastic reduction in  $q_{st}$  represents energeti-



**Figure 15.**  $\text{Li}^+$  decorated scaffold with (18, 18), 12 L nanotubes.

cally heterogeneous substrate and no sorbate–sorbate interaction, as explained in section 3.5. Li incorporation creates this heterogeneity with locations of high energy sites and low energy sites. Once the higher energy sites are filled at low pressure, the remaining low energy sites are filled at higher pressure. At 298 K the sites are energetically more homogeneous as represented by the almost flat lines for  $q_{\text{st}}$  with increased loading. But Li decorated scaffolds have higher  $q_{\text{st}}$  than bare scaffolds.

There is an important phenomena in some of the Li decorated structures. In some structures, as mentioned in various studies,<sup>21,37,39</sup> there is clustering of Li atoms and formation of  $\text{LiH}$ . Although we do not see such phenomena in our simulation, this is discussed in detail in the following paragraphs for clarification of certain issues.

We used Monte Carlo simulation with empirical force field to model the equilibrium sorption behavior of scaffold structures, whereas Liu et al.<sup>21</sup> and Zhao et al.<sup>37</sup> used the DFT method which is based on quantum calculation on electronic structure on a much smaller number of atoms. Use of DFT has enabled them to capture the Li clustering and metal–hydride formation phenomena. On the other hand, in our Monte Carlo simulation, the Dreiding force field which we used is not equipped to capture the atomic reaction (metal–hydride) phenomena; thus, we cannot directly comment on formation of metal–hydride in our structure. However, based on the available literature, we can make some relevant observations which will give some insight into whether there may be metal hydride formation phenomena in our structure or not. These are presented below.

There are quite a few studies like refs 21, 22, and 36–39 which comment on the optimum Li:C ratio (Li density) in carbon nanostructures, based on minimum total energy of the structure, number of Li aggregate formation, highest hydrogen binding, etc. Different optimum ratios have been reported, which are between 1:3 and 1:18, but most of them reported the optimum Li:C ratio to be around 1:6. Lithium graphite intercalated compounds having various Li concentrations (Li:C as 1:6–1:18) also have been prepared experimentally.<sup>40</sup> These indicate two things. First, these studies show that it is possible to prepare Li decorated CNT with a Li:C ratio of 1:6. Second, these indicate that different studies have found different optimum ratios, which may be attributed to the difference associated with the substrate molecular structure.

For example, Zhao et al.,<sup>37</sup> who did a DFT calculation on cointercalation of Li and small organic molecule on graphite, reported that a maximum Li containing graphite intercalated compound that they could prepare without Li clustering was of  $\text{Li}_4(\text{THF})\text{C}_{72}$  (where the Li:C ratio was 1:18). They found that at high Li ratios, there was a tendency to form Li clustering and Li-hydride formation. According to them, when the bond distance between Li atoms is around 2.8 Å, that indicates occurrence of Li clustering. Such Li clustering will eventually lead to Li-hydride formation in their structure. On the other hand, Liu et al.,<sup>21</sup> who also studied hydrogen storage in Li

dispersed carbon nanotubes using the DFT method, used a Li:C ratio of 1:8 without any  $\text{Li}^+$  clustering. Moreover Sun et al.,<sup>39</sup> who performed DFT calculation on Li coated fullerene, found an optimum Li:C ratio of 1:5 without Li clustering. Therefore it seems that the optimum Li:C ratio depends on the particular structure and is not a universal ratio. The notion of “high Li density” (expressed as Li:C ratio) which leads to hydride formation may be dependent on the particular structure and its chemical environment. Thus, it is possible that a particular Li:C ratio that is considered high for one structure (leading to hydride formation) may not be high enough to lead to a similar phenomenon in another structure. Thus, the ratio of 1:6 may not be necessarily considered as high enough in our CNT scaffolds to form metal hydride.

Furthermore, in our study, we found the optimum Li:C ratio to be 1:6 (150 Li), above which we observed a decrease in sorption capacity. In the case of 150 Li decorated scaffold (Li:C ratio 1:6), we observed that the average Li–Li distance was 4.81 Å (shortest being 2.66 Å observed for a few cases of Li atoms). This shortest distance is similar to the bond distance in a  $\text{Li}_2$  molecule,<sup>39</sup> which may indicate limited amount of Li clustering. However, this does not necessarily indicate metal hydride formation. The reason is explained below.

In our study, the minimum Li–H distance was  $\sim 3.4$  Å, which is larger than the Li–H bond distance for a  $\text{LiH}$  molecule ( $\sim 1.61$  Å).<sup>39</sup> Hydrogen was in the molecular form, and the bond distance between hydrogen atoms was maintained at 0.74 Å. In several studies,<sup>21,22,36–39</sup> it has been observed that hydrogen binds as a molecular form on Li intercalated or Li decorated structures. Thus, even though there is a limitation in our simulation method, we still believe that the hydrogen is adsorbed in the molecular form and there is no hydride formation. However, this needs further investigation.

**3.10. Sorption Capacity at 243 K.** The DOE target was already achieved by bare scaffolds at 77 K. So next we wanted to verify whether the presence of  $\text{Li}^+$  may improve the sorption capacity and help move toward the achievement of the DOE target. We conducted a sorption study for the (18, 18), 12 L tube scaffold with 150 Li atoms with stoichiometry  $\text{LiC}_6$ , to see the sorption capacity at 243 K ( $-30^\circ\text{C}$ ), which is the lowest temperature DOE target. For this study we have increased the van der Waals interaction cutoff to 15 Å. This scaffold achieves 5.84 total wt % at 100 bar (Figure 19).

We prepared two more (18, 18) tube scaffolds with (1) 200 Li placed outside surface of the tube wall and (2) in another case 150 Li at the outside surface and 50 Li at the inside surface of the tube. However, this high amount of Li did not increase sorption capacity but decreased it. So we considered the (18, 18), 12 L tube with 150 Li (Li:C ratio of 1.6) to be the optimum. For this scaffold, the system volumetric capacity reached 35.7 g/L, which is an improvement over the bare tubes (28.8 g/L). But this is lower than the DOE target (45 g/L).

#### 4. Summary and Concluding Remarks

Efficient storage of hydrogen is one key challenge for the hydrogen economy. Carbon nanotubes are considered as potential hydrogen storage materials because they have large surface areas and high adsorption capacities. However, single walled carbon nanotubes bundle up tightly, so most of their surface areas become inaccessible for adsorption. One way to improve the sorption capacity of these carbon nanotubes is to hold the tubes at a distance from each other in a scaffolded structure, so that their external sorption surfaces become accessible to hydrogen molecules.

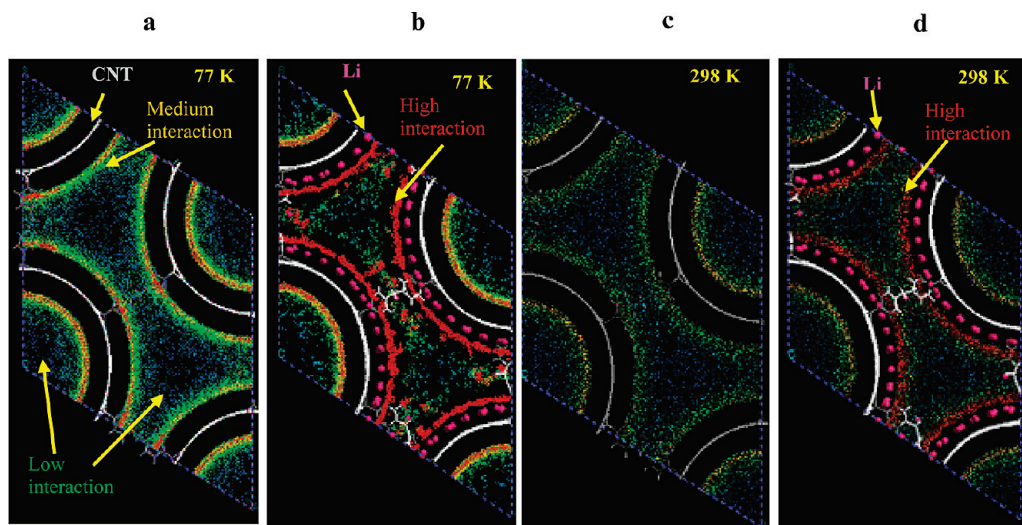


Figure 16. Mass density plot for (18, 18), 12 L at 77 and 298 K, 1 atm, with and without Li.

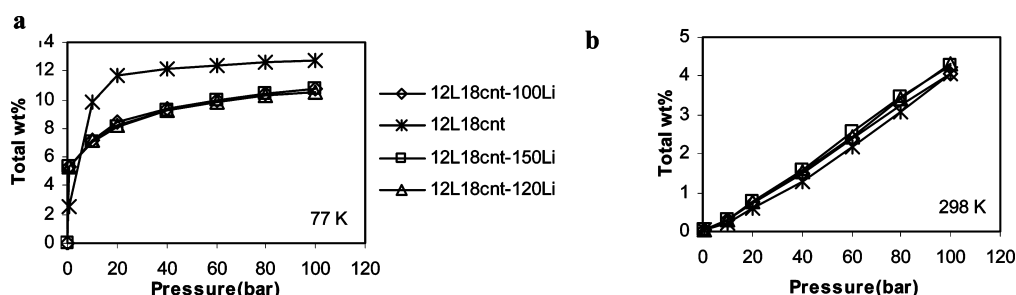


Figure 17. Total capacity of  $\text{Li}^+$  decorated scaffolds at (a) 77 K and (b) 298 K.

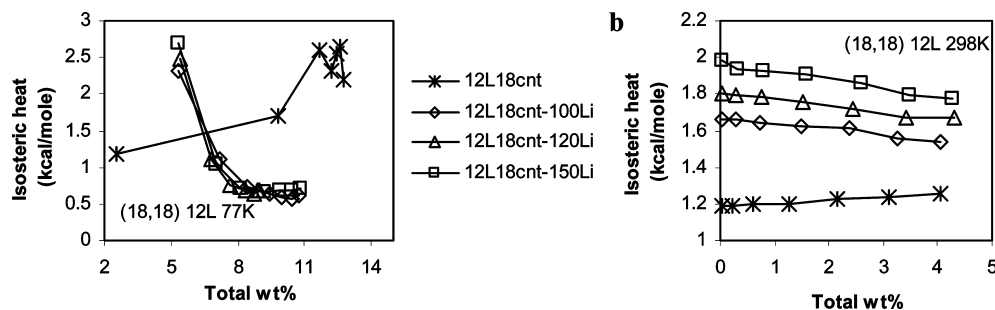


Figure 18. Isosteric heat of  $\text{Li}^+$  decorated (18, 18) scaffold at (a) 77 K and (b) 298 K.

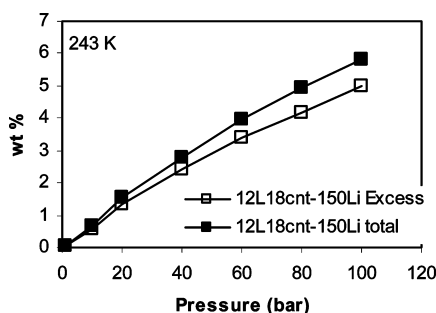


Figure 19. Sorption capacity at 243 K ( $-30^\circ\text{C}$ ).

With the of goal improving the sorption capacities of such scaffolds, we analyze the effect of linker densities, tube diameter, carbon nanotube surface functionalization, and Li decoration on sorption capacity. We studied sorption capacity of scaffolds with a range of volume and surface areas, using molecular dynamics and grand canonical Monte Carlo simulation. For these studies we prepared SWNT scaffolds that had different diameters and were covalently connected by methylene–dianiline cross-

linker after every 4th, 7th, 9th, and 12th layers of benzene rings. The scaffolds with larger diameter tubes and wide linker spacing showed higher sorption capacities. At 77 K, several of these scaffolds achieved and exceeded DOE gravimetric and volumetric hydrogen storage targets. We studied one zigzag tube as a test case and found that chirality may have some effect on sorption capacity at lower temperature (77 K) but has no effect at room temperature. This needs further investigation. We found that additional functionalization of the tube walls had a detrimental affect on sorption capacity due to steric hindrance and adsorption space reduction caused by bulky functional groups. On the other hand, incorporation of  $\text{Li}^+$  ions on the outer tube surface increased sorption capacity by increasing the adsorption interaction energy. At 243 K,  $\text{Li}^+$  incorporated (18, 18), 12 L scaffold reached a total capacity of 5.84 wt %. However, actual performance of this  $\text{Li}^+$  incorporated scaffold has to be experimentally measured in the laboratory to confirm this. Future studies may be conducted to see the effect of other transition metals in the scaffolds.



The focus of this study was to characterize the CNT scaffold as a sorption material. Hence, we did not plan to study the desorption kinetics in this current work. This may be addressed in the future. However, we see the binding energy is not more than  $\sim 11$  kJ/mol (in the case of Li decorated tube); therefore, we can expect that hydrogen will be labile and will be desorbed easily from the scaffold.

**Acknowledgment.** This work is supported in part by grants from the NSF (IMI, IGERT) and ONR, and computations were carried out at the Laboratory of Computational Nanomaterials, Laboratory of Molecular Simulations, and TAMU Supercomputing Center. We are thankful to our unknown reviewers who have posed critical comments and thus have enabled us to improve the quality of the paper.

## References and Notes

- (1) Schlapbach, L.; Züttel, A. *Nature* **2001**, *414*, 353–358.
- (2) Züttel, A. *Naturwissenschaften* **2004**, *91* (4), 157–172.
- (3) Satyapal, S.; Petrovic, J.; Read, C.; Thomas, G.; Ordaz, G. *Catal. Today* **2007**, *120* (3–4), 246–256.
- (4) Dillon, A. C.; Jones, K. M.; Bekkedahl, T. A.; Kiang, C. H.; Bethune, D. S.; Heben, M. J. *Nature* **1997**, *386*, 377–379.
- (5) Ströbel, R.; Garche, J.; Moseley, P. T.; Jörissen, L.; Wolf, G. *J. Power Sources* **2006**, *159* (2), 781–801.
- (6) Liu, C.; Fan, Y. Y.; Liu, M.; Cong, H. T.; Cheng, H. M.; Dresselhaus, M. S. *Science* **1999**, *286* (5442), 1127–1129.
- (7) Chen, P.; Wu, X.; Lin, J.; Tan, K. L. *Science* **1999**, *285* (5424), 91–93.
- (8) Darkrim, F.; Levesque, D. *J. Chem. Phys.* **1998**, *109* (12), 4981–4984.
- (9) Murata, K.; Kaneko, K.; Kanoh, H.; Kasuya, D.; Takahashi, K.; Kokai, F.; Yudasaka, M.; Iijima, S. *J. Phys. Chem. B* **2002**, *106*, 11132–11138.
- (10) Kuc, A.; Zhechkov, L.; Patchkovskii, S.; Seifert, G.; Heine, T. *Nano Lett.* **2007**, *7* (1), 1–5.
- (11) Dimitrakakis, G.; Tylianakis, E.; Froudakis, G. *Nano Lett.* **2008**, *8* (10), 3166–3170.
- (12) Kostov, M. K.; Cheng, H.; Cooper, A. C.; Pez, G. P. *Phys. Rev. Lett.* **2002**, *89* (14), 146105–1–4.
- (13) Pradhan, B. K.; Sumanasekera, G. U.; Adu, K. W.; Romero, H. E.; Williams, K. A.; Eklund, P. C. *Physica B (Amsterdam, Neth.)* **2002**, *323* (1–4), 115–121.
- (14) Leonard, A. D.; Hudson, J. L.; Fan, H.; Booker, R.; Simpson, L. J.; O'Neill, K. J.; Parilla, P. A.; Heben, M. J.; Pasquali, M.; Kittrell, C.; Tour, J. M. *J. Am. Chem. Soc.* **2009**, *131* (2), 723–728.
- (15) Wang, Q.; Johnson, K. *J. Phys. Chem. B* **1999**, *103*, 4809–4813.
- (16) Wang, Q.; Johnson, K. *J. Chem. Phys.* **1999**, *110*, 577–586.
- (17) Darkrim, F.; Levesque, D. *J. Phys. Chem. B* **2000**, *104*, 6773–6776.
- (18) Weck, P. F.; Kim, E.; Balakrishnan, N.; Cheng, H.; Yakobson, B. I. *Chem. Phys. Lett.* **2007**, *439* (4–6), 354–359.
- (19) Shirashi, M.; Takenobu, T.; Ata, M. *Chem. Phys. Lett.* **2003**, *367*, 633–636.
- (20) Bahr, J. L.; Tour, J. M. *J. Mater. Chem.* **2002**, *12*, 1952–1958.
- (21) Liu, W.; Zhao, Y. H.; Li, Y.; Jiang, Q.; Lavernia, E. J. *J. Phys. Chem. C* **2009**, *113* (5), 2028–2033.
- (22) Deng, W.-Q.; Xu, X.; Goddard, W. A. *Phys. Rev. Lett.* **2004**, *92* (16), 166103–1–4.
- (23) Yildirim, T.; Ciraci, S. *Phys. Rev. Lett.* **2005**, *94*, 175501–1–4.
- (24) Cheng, H.; Cooper, A. C.; Pez, G. P.; Kostov, M. K.; Piotrowski, P.; Stewart, S. J. *J. Phys. Chem. B* **2005**, *109*, 3780–3786.
- (25) Materials Studio, Accelrys, San Diego, CA.
- (26) Cerius2, Accelrys, San Diego, CA.
- (27) Andzelm, J.; Piela, L. *J. Phys. C: Solid State Phys.* **1977**, *10*, 2269–2283.
- (28) Gao, G.; Cagin, T.; Goddard, W. A., III. *Phys. Rev. Lett.* **1998**, *80* (25), 5556–5559.
- (29) <http://webbook.nist.gov/chemistry/fluid/>.
- (30) Yang, R. T. *Carbon* **2000**, *38*, 623–641.
- (31) Sircar, S.; Cao, D. V. *Chem. Eng. Technol.* **2002**, *25* (10), 945–948.
- (32) Zhang, X.; Cao, D.; Chen, J. *J. Phys. Chem. B* **2003**, *107*, 4942–4950.
- (33) Benard, P.; Cahine, R. *Int. J. Hydrogen Energy* **2001**, *26*, 849–855.
- (34) Mavrandonakis, A.; Klontzas, E.; Tylianakis, E.; Froudakis, G. E. *J. Am. Chem. Soc.* **2009**, *131* (37), 13410–13414.
- (35) Simonyan, V. V.; Diep, P.; Johnson, J. K. *J. Chem. Phys.* **1999**, *111* (21), 9778–9783.
- (36) Blomqvist, A.; Moyses Araujo, C.; Srepusharawoot, P.; Ahuja, R. *Proc. Natl. Acad. Sci. U.S.A.* **2007**, *104* (51), 20173–20176.
- (37) Zhao, Y.; Kim, Y.-H.; Simpson, L. J.; Dillon, A. C.; Wei, S.-H.; Heben, M. J. *Phys. Rev. B* **2008**, *78*, 144102–5.
- (38) Han, S. S.; Goddard, W. A., III. *J. Am. Chem. Soc.* **2007**, *129*, 8422–8423.
- (39) Sun, Q.; Jena, P.; Wang, Q.; Marquez, M. *J. Am. Chem. Soc.* **2006**, *128*, 9741–9745.
- (40) Ohzuku, T.; Iwakoshi, Y.; Sawai, K. *J. Electrochem. Soc.* **1993**, *140* (9), 2490–2498.

JP1027806